2 Experimental details

2.1 SPLEEM

The spin-polarized low energy electron microscopy (SPLEEM) measurements have been performed at the National Center of Electron Microscopy (NCEM [110]) at the Lawrence Berkeley National Laboratory in Berkeley, California, USA. Besides the principles of the interaction of spin-polarized low energy electrons with matter, the mode of operation of the SPLEEM instrument is described in section 2.1.1. A comparison with other magnetic domain imaging methods follows in section 2.1.2.

2.1.1 Mode of operation

Magnetic contrast (MC) in SPLEEM is based upon the exchange interaction $E_{ex} = \sum_{ij} J(\mathbf{r}_i - \mathbf{r}_j)\ \mathbf{s}_i \cdot \mathbf{s}_j$ between the incident electrons with spin $\mathbf{s}_i$ and the target electrons with spin $\mathbf{s}_j$ at their positions $\mathbf{r}_i$ and $\mathbf{r}_j$, J being the exchange coupling constant. In regions with preferred spin alignment $\mathbf{s}_j$ a non-zero magnetization $\mathbf{M} \propto \sum_j \mathbf{s}_j$ exists, which gives rise to a magnetic contribution proportional to $\mathbf{P} \cdot \mathbf{M}$ to the scattered signal if the incident beam is spin-polarized with a polarization $\mathbf{P} \propto \sum_i \mathbf{s_i}$ [21]. In a crystal the occurrence of magnetic contrast can also be explained in terms of the spin-dependent band structure in which spin-up and spin-down electrons have different energies. This is illustrated in Fig. 2.1 (a) where, as an example, the spin-down and spin-up bands above the vacuum energy, which are the relevant bands for the incident electrons, are shown for normal incidence on the [0001] surface of hcp Co (Ref. [111]). For energies of the incident electrons below ≈1 eV the incident beam is reflected because there are no allowed states in the crystal independent of the spin orientation of the electrons. The strongest effects on the reflectivity appear when states are unavailable for electrons with a certain polarization, while states are available for electrons with the same energy but opposite polarization. Spin-down electrons with an energy between 1 and 2 eV above the vacuum level, which corresponds to the gap between the spin subbands in Fig. 2.1 (a), cannot exist in the crystal and are therefore totally reflected, whereas the spin-up electrons are able to enter the crystal band structure and are poorly reflected [111]. When $\mathbf{P}$ is adjusted by the illumination optics, the reflectivity depends on the orientation of $\mathbf{M}$ with respect to $\mathbf{P}$ and therefore, the magnetic domain structure can be imaged with high contrast in this energy range. Above the

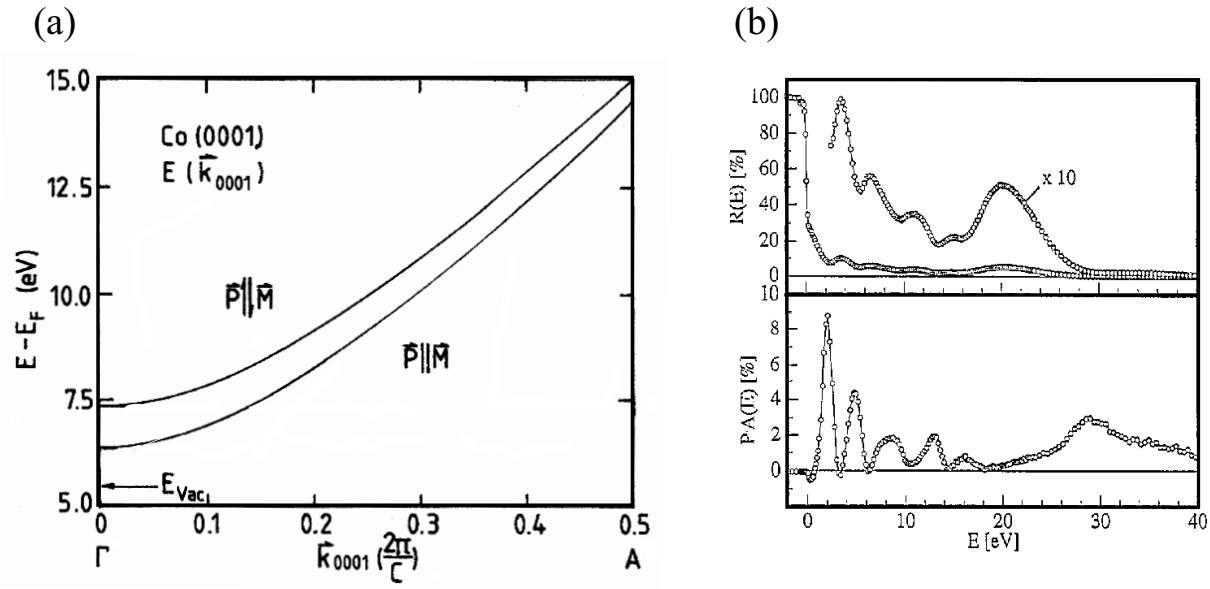

Figure 2.1: (a) Band structure of Co above the vacuum level in the [0001] direction (From [111]). (b) Oscillation of the measured reflectivity R (top) and asymmetry PA from a 6 ML Co/W(110) thin film as a function of the energy of the electrons. (From [112]).

upper band in Fig. 2.1, allowed states exist for both spin orientations and the magnetic contrast decreases with increasing energy until the next spin-dependent band discontinuity is reached. Some magnetic contrast, however, remains which can be enhanced by subtracting two images with opposite spin directions [113]. In the individual images also topographic contrast occurs. Since the topographic contrast is independent of $\mathbf{P}$ and the magnetic contrast is proportional to $\mathbf{P} \cdot \mathbf{M}$ the resulting images reveal pure magnetic contrast. If $I^{\uparrow}$ and $I^{\downarrow}$ are the intensities at the same site in two images recorded with opposite $\mathbf{P}$, and the images are normalized by their sum, an image is obtained which is proportional to the reflectivity asymmetry A,

$$P_0 A = \frac{I^{\uparrow} - I^{\downarrow}}{I^{\uparrow} + I^{\downarrow}} \tag{2.1}$$

P_0 being the polarization of the incident beam ($\approx 20 - 25\%$). Since spin-dependent magnetic contrast is determined by the spin-dependent band structure, the exchange asymmetry oscillates with energy. In ultrathin films, where the electron wavelength and penetration depth becomes comparable to the film thickness at very low energies, there is another important consequence of the fact that the k-values are different of the two bands at a given energy, namely the resonance conditions for standing waves which arise in such films are different. The resulting oscillations of the asymmetry due to this quantum size effect [114,115] is displayed in Fig. 2.1 (b). The quantum size oscillations vanish if the film thickness exceeds about 20 ML because their frequency increases rapidly with increasing thickness. The reflectivity oscillation due to the band structure, however, remains [21].

In order to maximize the magnetic contrast it is desirable to align $\mathbf{P}$ parallel to any local

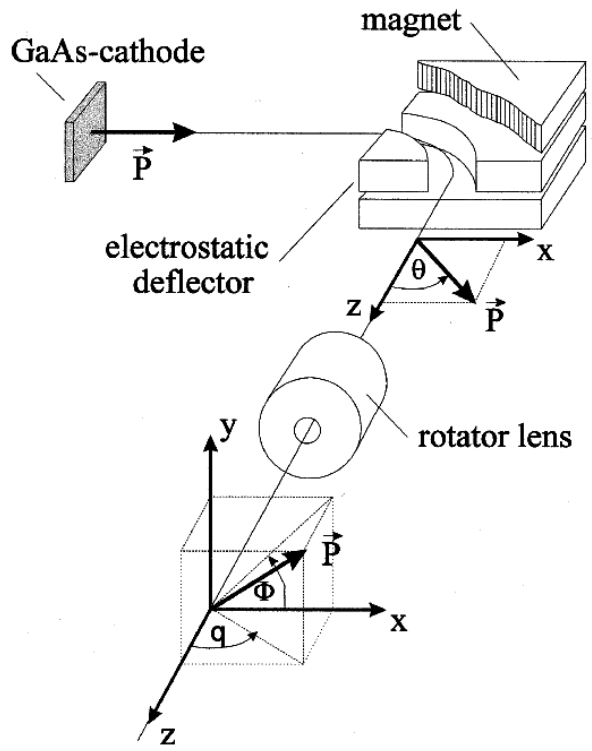

Figure 2.2: Schematic arrangement of the electrostatic and the magnetic deflectors of the SPLEEM instrument, which are used to bend the path of the laser excited electrons onto the microscope axis z. By means of the deflectors in combination with a magnetic rotator lens the direction of the polarization vector $\mathbf{P}$ is adjusted with respect to the (x, y) sample plane. (From [20]).

magnetization $\mathbf{M}$, i. e. to rotate $\mathbf{P}$ in any direction in space. The setup which allows this rotation of $\mathbf{P}$ by electron optical means is the polarization manipulator shown schematically in Fig. 2.2 [20]. With the photon energy slightly larger than the bandgap of the GaAs-based semiconductor cathode, electrons are excited by circularly polarized light from the spin-split levels at the top of the valence band. Transition probabilities lead to an unequal population of the two spin states in the conduction band [116,117]. Normally, conduction electrons are not able to escape from the crystal due to the high electron affinity, but emission can be enhanced by lowering the vacuum level below the minimum of the bulk conduction band. This negative electron affinity condition is generated by depositing a caesium-oxide layer onto the crystal surface [118]. The excited electrons are polarized longitudinally by the circularly polarized laser beam. A 90°-deflection by the electrostatic sector field does not influence the polarization vector $\mathbf{P}$. Consequently, $\mathbf{P}$ is oriented normal to the propagation directly after the sector field. If the electrostatic sector is turned off and the deflection is attained by the magnetic sector field, $\mathbf{P}$ follows the trajectory of the electron as anticipated by the equation of motion for the polarization [119], resulting in a longitudinally polarized beam [111]. By superposition of the electric and the magnetic deflection fields, any orientation of $\mathbf{P}$ can be obtained between $0° < \theta < 90°$ within the (x, z)-plane according to Fig. 2.2. After passing the 90°-deflector the electrons enter a magnetic lens, whose longitudinal magnetic field causes a precession of the transverse component of $\mathbf{P}$ around the beam axis when the lens is excited. A combination of both the magnetic and the electric deflector as well as the magnetic rotator lens allows to rotate

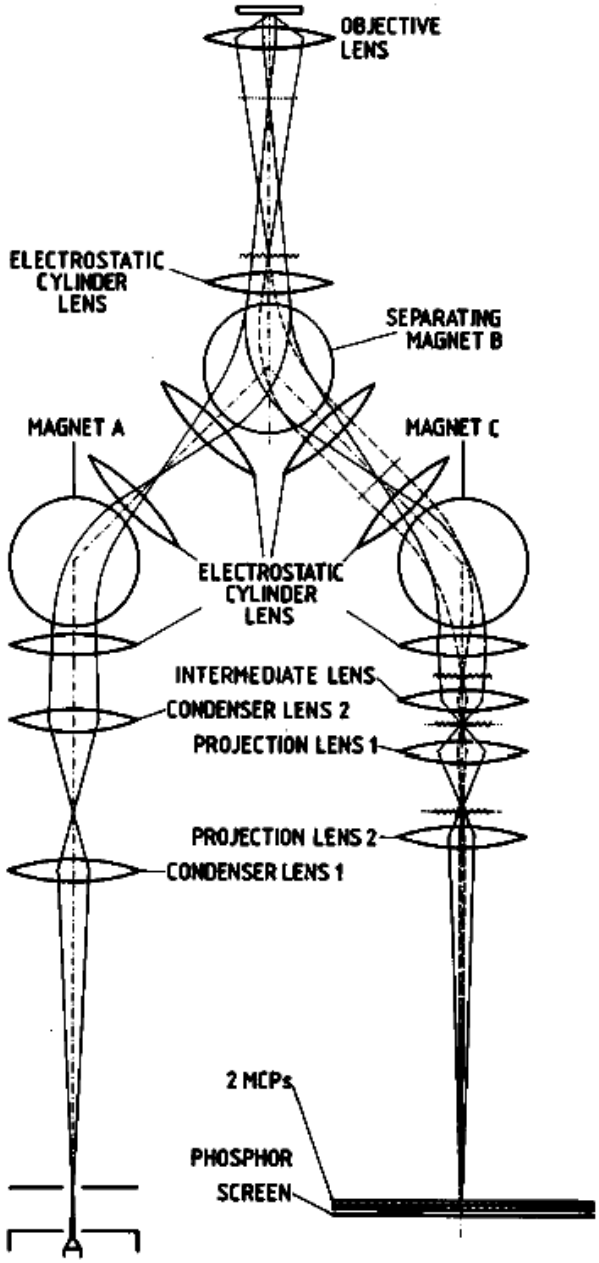

Figure 2.3: Electron optical schematic diagram showing the trajectories (dashed-dotted line) within the illumination column (left hand side) and the imaging column (right hand side). On the left hand side the solid lines shows optimum illumination, on the right hand side they represent rays in LEED mode, whereas the dashed lines stand for rays in LEEM mode. The sample resides in front of the objective lense. The low energy electrons are elastically backscattered into the direction of the imaging column. (From [120]).

$\mathbf{P}$ into any desired direction.

The trajectories of the electrons through the microscope after passing the spin manipulator is shown in Fig. 2.3. The spin-polarized electron source resides near the lower left part of the sketch, which is the entrance of the illumination column. Electrostatic lenses are used to focus the beam, and sector magnets deflect the beam twice before it passes the electrostatic tetrode objective lens [120]. Due to the variation in focal length with energy and the energy spread of the electron source, electron optical lenses focus electrons poorly at energies much less than a few keV [121]. Therefore, the electron optical columns are operated at a high energy of the electrons of 3 keV. To obtain low energy electrons at the sample, a strong, homogeneous retarding electric field between the objective lens and the sample, which is at ground potential,

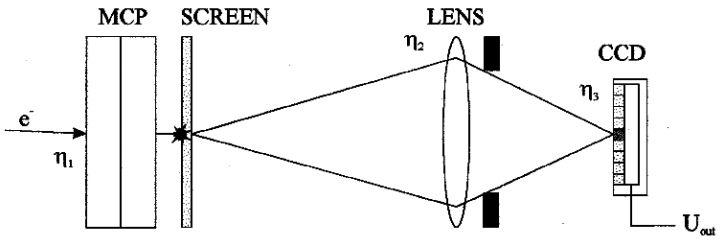

Figure 2.4: Simplified sketch of the detection system. The backscattered electrons are multiplied in two coupled multichannel plates (MCP) and the resulting image is displayed on a phosphorous screen, which is observed by a CCD camera. (From [111]).

decelerates the electrons to an energy of typically below 10 eV before they reach the sample at normal incidence. The distance between the sample surface and the objective lens is about 1.5 mm. The potentials of the first lens of the objective and of the rest of the instrument are 12.5 kV and 3 kV, respectively. Elastically backscattered electrons are accelerated again toward the imaging column, where electrostatic lenses and bending magnets finally guide the electron beam toward a multichannel plate (MCP). The specular beam finally forms a magnified real space image on a phosphorous screen, which is observed by a CCD camera, as sketched in Fig. 2.4. In order to prevent any disturbance of the electron beam by the magnetic field of the earth and electromagnetic radiation of the environment, the microscope resides within in a μ-metal shielding. At the site of the electron source the magnetic field is compensated by means of three pairs of Helmholtz coils. More details about the operating mode of the SPLEEM can be found elsewhere [20,21,111,120,122].

The contrast mechanism in low energy electron microscopy (LEEM) can be divided into two classes, i. e. diffraction and phase contrast. Diffraction contrast arises from local variations of the structure factor. In bright-field imaging at normal incidence it is due to geometric differences between different structural phases, for example, surface reconstructions of atoms on a clean crystalline substrate.

Two important mechanisms of the phase contrast are step contrast and quantum size contrast; both provide atomic resolution perpendicular to the surface. On surfaces with terraces separated by atomic steps the geometric step contrast arises from the interference of electron waves being reflected from opposite sides of a step. Due to the difference of the path lengths of these electrons, the interference arises from the acquired phase shift. At energies below 10 eV the wave length of the electrons is on the order of the atomic step height and thus small changes in the energy lead to a wide range of phase shifts, and consequently to various interference conditions [114]. The quantum size contrast is based on the quantum size effect (QSE), which results from the interference between the electron waves being reflected from the surface of a thin film and from the substrate, respectively. The two phase contrast mechanisms are depicted in Fig. 2.5. To find the optimum magnetic contrast for the Ni/Cu(100) films several series of

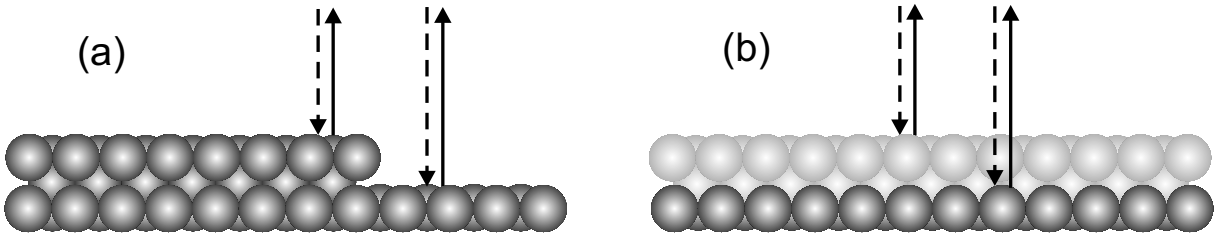

Figure 2.5: Mechanisms of the LEEM phase contrast. (a) step contrast, (b) quantum size contrast.

SPLEEM images at different electron energies and different Ni thicknesses were taken. The exchange asymmetry oscillates between 4 and 11 eV with a maximum at about 9.2 eV. Note, that our energy scale is measured with respect to the Fermi level, i. e. to obtain the electron kinetic energy, the difference in the work functions of the sample and the cathode must be subtracted (about 3 eV). At about 4.5 eV the MC is reversed and much weaker than at 9.2 eV. Between 5 and 8 ML the maximum shifted only by a few tenth of 1 eV. All Ni domain images presented in this work were recorded at $E = 9.5$ eV. The same procedure was done for Fe/Cu(100) films with the result that optimum magnetic contrast was achieved at $E = 4.5$ eV. At this energy of the electrons, images of Fe domains were recorded. In order to image the step edges of the bare Cu crystal with high structural contrast with LEEM, an energy of the electrons of 4.9 eV turned out to be optimal for the used substrates.

2.1.2 Comparison with other domain imaging methods

Various approaches to magnetic microscopy have lead to different techniques to image magnetic domains. Since different physical phenomena are exploited, all methods presented in the following have advantages and disadvantages. Generally, there are two categories of imaging methods, some probing the far-field, and others scanning the near-field. Far-field techniques include electron-, magneto-optical-, and x-ray microscopy, whereas magnetic force microscopy (MFM) as well as magneto-optical scanning near-field (M-SNOM) and spin-polarized scanning tunnelling microscopy (SP-STM) belong to the near-field techniques. In the following the different features of the domain imaging methods are described and summarized in table 2.1.

Magneto-optical domain imaging in reflection and transmission, exploiting the magneto-optical Kerr effect (MOKE) [123] and the Faraday effect [124], respectively, is well established nowadays. Both effects are based on small rotations of the polarization plane of the light, and the domain pattern becomes viewable in the polarizing microscope. Since few samples are transparent, the Faraday effect can rarely be used, whereas the Kerr effect is applied in both its longitudinal and transverse mode to image the in-plane and out-of-plane components of the magnetization. In a calibrated computer-based Kerr microscope a quantitative determination of the magnetization direction and quantitative evaluation of domain wall parameters is possible

Table 2.1: Domain imaging methods classified into far-field (upper table) and near-field methods (lower table). (In part taken from [127]).

Imaging technique	Resolution	Special features
Lorentz microscopy	$\leq$ 10 nm [17]	intermediate external magnetic fields H_{ex}
SEMPA	$\geq$ 10 nm [128]	determination of magnetization direction
X-PEEM	$\geq$ 20 nm [129]	element-specific imaging
SPLEEM	$\geq$ 10 nm [130]	topography and determination of magnetization direction
Magneto-optical microscopy	$\geq$ 300 nm [127]	strong external magnetic fields
MFM	$\geq$ 10 nm [127]	H_{ex}, quantitative method
M-SNOM	$\geq$ 50 nm [127]	topography and magnetic contrast
SP-STM	$<$1 nm [131]	H_{ex} if antiferromagnetic tips used

[125]. The observation of domain wall dynamics in an applied magnetic field with up to 5000 frames per second on a 100 μm scale has been reported [126]. The possibility to apply high or low temperatures as well as mechanical stress and almost unlimited magnetic fields during the domain observation is a clear benefit of this method. As a drawback it should be mentioned that the lateral resolution is limited corresponding to an optical resolution of about 300 nm, and an electronic contrast enhancement may be necessary which is often associated with additional equipment [17].

In Lorentz microscopy a transmission electron microscope (TEM, 100-1000 keV) is used to image magnetic domains with high resolution better than 10 nm. This method is based on the deflection of transmitted electrons through a magnetic thin film due to the Lorentz force, which is proportional to the local magnetic induction. Domains can be imaged with high contrast and sensitivity even to small variations of the magnetization. The interaction between domain walls and lattice defects can be studied. However, a TEM equipment optimized for magnetic investigations is generally not optimal for other purposes. Manipulation of the sample by mechanical stresses or magnetic fields is difficult, and for measurements of the perpendicular component of the magnetization the sample must be tilted.

In secondary electron microscopy with polarization analysis (SEMPA) [132] the magnetic sample surface is scanned with a narrow electron beam, which excites secondary electrons of up to 50 eV near the surface of the sample. These electrons, which are spin-polarized parallel to the magnetization orientation of the site of their origin, are collected and accelerated toward a spin-detector, such as a Mott-detector. With a lateral resolution down to 10 nm [133] and the possibility to image the sample's topography and to simultaneously detect all three magnetiza-

tion components quantitatively [134,135] SEMPA is a powerful technique for domain imaging purposes. Due to the low efficiency of commonly used polarization detectors long exposure times up to several minutes are normally required. The sampling depth in metals is about 20 nm.

Magnetic force microscopy (MFM) is based on an atomic force microscope (AFM). Unlike AFM, in MFM a magnetized vertically vibrating cantilever tip is scanned in close proximity to the surface over the sample, detecting the magnetic dipole field. MFM images result from local frequency variations of the tip due to the presence of magnetic field gradients caused by the magnetic stray field of domain boundaries. The long range dipole-dipole-interaction limits the resolution to typically ≈50 nm, which can be improved by very small tip dimensions to ≈10 nm. A drawback is the difficulty of extracting quantitative information like the magnetization directly from MFM images, although there exist also various quantitative MFM methods to calibrate the tip, to calculate the stray field and to simulate MFM data [136–139]. Moreover, the magnetic stray field of the tip may modify the local domain structure of soft magnetic samples and the magnetization of the tip can change in the presence of an external magnetic field [127].

The basis of magnetic photoemission electron microscopy (X-PEEM) is x-ray magnetic circular dichroism (XMCD), which will be discussed in detail in section 2.2. Photoelectrons excited from core levels by circularly polarized x-rays are detected in the microscope. Pure magnetic contrast remains after subtracting two images taken with light of opposite helicity and an energy corresponding for example to the L_3-edge of the sample material. The most striking advantage of X-PEEM is element-specific imaging, which is obtained from core-level selectivity by tuning the excitation to the absorption edge of the desired element in a heterogeneous sample [140]. Recent time-resolved X-PEEM measurements demonstrated the capability of taking a series of images in nanosecond-intervals after a high field pulse [141]. One drawback is that synchrotron based x-rays are needed for X-PEEM measurements.

Scanning near-field magneto-optical microscopy (M-SNOM) uses either linear magneto-optical effects (Kerr or Faraday effect) or nonlinear effects by scanning a near-field detector or, alternatively, a small-aperture light source of sub-wavelength size in close proximity to the surface of the sample. Besides the impressive resolution of ≈50 nm, a further advantage is that surface topography and optical image are recorded at the same time allowing for correlations between structure and magnetism.

The highest lateral resolution is achieved by spin-polarized scanning tunnelling microscopy (SP-STM). It is usually not better than 1 nm [142,143], however, recently an atomic-scale SP-STM has been demonstrated to resolve magnetic structure of the order of 0.5 nm [131]. In a SP-STM magnetic contrast is obtained through the spin-dependent tunnelling probability between a magnetic sample and a tip, which acts as a source of spin-polarized electrons. By using non-magnetic tips, which are coated with an antiferromagnetic material, e. g. Cr [144], an external

magnetic field can be applied during the measurement.

The mode of operation of SPLEEM has already been explained in the previous section. One benefit of this technique is the combination of topographic contrast, which is contained in every LEEM image due to the use of surface sensitive low energy electrons, and the pure magnetic contrast arising from the subtraction of two corresponding LEEM images as described above. By this virtue the origin of possible domain wall pinning or the correlation between magnetic domain formation and the substrate morphology can be clarified in every domain image. In addition, lateral resolution on the order of 10 nm for both LEEM and SPLEEM mode allows for the investigation of domain walls in ultrathin magnetic films, which have typical wall widths of 1-1000 nm. The possibility of real-time imaging, recording up to 10 images per second during thin film growth at low or high temperatures, makes SPLEEM a very flexible method to image the dynamics of domain formation. In addition, the application of external magnetic fields of $\approx$4 kA/m [1] perpendicular to the sample surface has been successfully performed without image distortion [145]. Another important advantage is that all three magnetization components can be detected within a few seconds, which was the decisive reason for this work to study the spin-reorientation transition in ultrathin Ni- and Fe/Ni-films on Cu(100) by the means of SPLEEM. A shortcoming of SPLEEM, however, is that the domain imaging is not element-specific, which would be desirable if multilayers or thin film alloys are to be studied.

2.2 XMCD

The x-ray magnetic circular dichroism (XMCD) technique is based on changes of the absorption cross section for left and right circularly polarized light, depending on the electronic band structure, which determines the magnetic properties of the absorbing material. XMCD is defined as the difference between the absorption spectra of left and right circularly polarized x-ray light for a static magnetic field along the incident axis of the photons. Following the definition in optics left (right) polarized light corresponds to a $+\hbar$ ($-\hbar$) helicity. For circularly polarized light the selection rules for an electric dipole transition from an atomic-like core state of the quantum numbers s, l, j and m according to the Wigner-Eckart theorem are given by:

$$\Delta s = 0, \quad \Delta l = \pm 1, \quad \Delta j = 0, \pm 1, \quad \Delta m = \begin{cases} +1 \text{ , left circular} \\ -1 \text{ , right circular} \end{cases} \tag{2.2}$$

where $\Delta s = 0$ means that a spin-flip during the transition is not allowed. This orbital-selective character of the x-ray absorption is sketched in Fig. 2.6 (a).

The basic principle of the XMCD effect at the L_3 and L_2 edges can be explained with the two-step model [146]. In the first step a circularly polarized photon excites a core electron from

[1] 4 kA/m $\approx$ 50 Oe

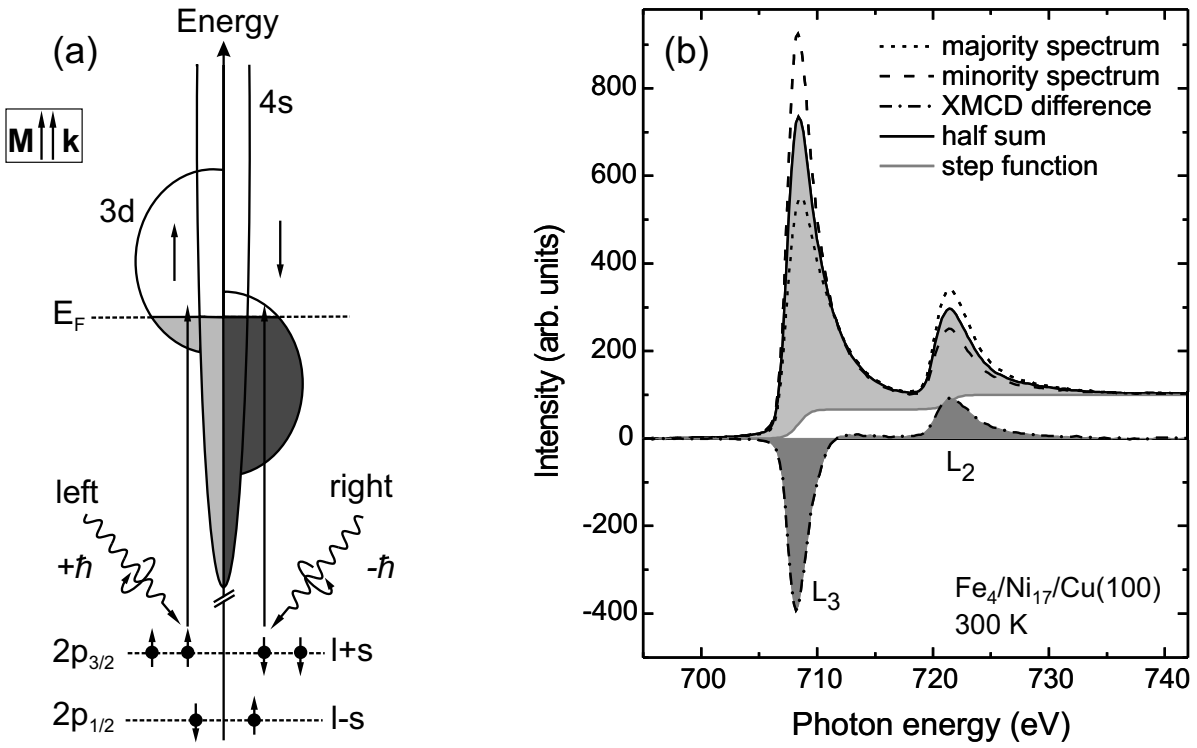

Figure 2.6: (a) Schematic of the x-ray magnetic circular dichroism at the $L_{2,3}$ edges of $3d$ transition metals. At the L_3 edge ($j = l + s$) the absorption of left (right) circularly polarized light causes a spin-selective excitation of photoelectrons from the spin-orbit split $2p_{3/2}$ core state to the exchange split $3d$ valence band which acts as a spin detector. Due to the imbalance of the unoccupied spin-up and spin-down states of the d band the absorption cross section for $+\hbar$ helicity is larger than for $-\hbar$. The effect reverses at the L_2 edge due to the opposite spin-orbit coupling ($j = l - s$). (b) The XMCD difference spectrum of an $Fe_4/Ni_{17}/Cu(100)$ film is obtained by subtracting the minority spectrum from the majority spectrum. The orbital (μ_L) and the spin (μ_S) moment can be determined by applying the magneto-optical sum rules after subtraction of the double step function from the half-sum spectrum.

the p-shell, which is split by the spin-orbit interaction into $2p_{3/2}$ (L_3) and $2p_{1/2}$ (L_2). At the L_3 and L_2 edges $\mathbf{l}$ and $\mathbf{s}$ are coupled parallel and antiparallel, respectively. The angular momentum of the photon is transferred to both the orbital and spin degree of freedom of the excited electron. At the L_3-edge ($j = l + s$) the absorption of photons with the helicity $+\hbar$ will mainly excite spin-up photoelectrons, since the transition probability is maximum for a parallel alignment of $\mathbf{l}$, $\mathbf{s}$ and $+\hbar$, whereas spin-down photoelectrons dominate the excitations with right circularly polarized light ($-\hbar$). Due to the opposite spin-orbit coupling ($j = l - s$) at the L_2-edge the resulting spin-polarization of the photoelectrons reverses for excitations from the $2p_{1/2}$ states compared to those from the $2p_{3/2}$ states.

In the second step the spin-up (spin-down) photoelectrons are excited into unoccupied spin-up (spin-down) states of the $3d$-valence band above the Fermi level. The $3d$-band can thus be considered as a sensitive "spin-detector" for spin-polarized photoelectrons. Setting the mag-

netization of the d-band parallel to the direction of the wave vector $\mathbf{k}$, the occupation of the spin-down states is larger than that of the spin-up states.

Due to the spin conservation ($\Delta s = 0$) the photoelectrons excited from $2P_{3/2}$ ($2P_{1/2}$) by photons of $+\hbar$ helicity probe mostly the spin-up (spin-down) states above the Fermi level. Consequently, the absorption of left circularly polarized x-rays will be enhanced at the L_3 edge and reduced at the L_2 edge according to the exchange-split $3d$-states. The absorption of right circularly polarized x-rays results in the opposite effect. This difference in absorption is the x-ray magnetic circular dichroism, which is conventionally defined as

$$\Delta\mu(E) \;=\; \mu^{+}(E) - \mu^{-}(E) \tag{2.3}$$

where μ^{+} and μ^{-} indicate the absorption of right and left circular polarized light. Accordingly, the dichroism effect reflects the spin imbalance of the exchange-split $3d$-band, and it is proportional to the difference in the unoccupied spin-up and spin-down states, i. e. to the spin magnetic moment. In order to obtain the XMCD spectra, one may also change the direction of the magnetization with respect to a fixed $\mathbf{k}$ instead of changing the helicity of the x-ray beam.

Fig. 2.6 (b) shows the two absorption spectra according to μ^{+} and μ^{-}, their half sum, which is the isotropic absorption cross section, the double step function and the resulting XMCD difference spectrum determined for the bilayer system Fe_4/Ni_{17}/Cu(100) at normal incidence of the circularly polarized x-ray. The indices denote the layer thicknesses in monolayers.

2.2.1 Determination of magnetic moments using “sum rules”

In contrast to polarized neutron diffraction (PND) [147] or SQUID magnetometry [148] the total magnetic moment cannot be determined directly from XMCD measurements. The separate values of the spin μ_S and the orbital μ_L magnetic moment are determined by applying the XMCD sum rules. The magneto-optical sum rules, which yield directly the average expectation values of the ground state of the orbital angular momentum operator $\langle L_Z \rangle$, as well as the spin momentum operator $\langle S_Z \rangle$ and magnetic dipole operator $\langle T_Z \rangle$ acting on the shell which receives the photoelectron in the final state, were developed by Thole *et al.* [149] and Carra *et al.* [150], respectively. From these sum rules the magnetic moments are determined as follows:

- the orbital magnetic moment: $\mu_L = -\frac{\mu_B}{\hbar} \langle L_Z \rangle$
- the spin magnetic moment: $\mu_S = -\frac{2\mu_B}{\hbar} \langle S_Z \rangle$
- the magnetic dipole moment: $\mu_T = +\frac{\mu_B}{\hbar} \langle T_Z \rangle$

where $\langle T_Z \rangle$ provides a measure of the anisotropy of the spin density [150]. For atoms with cubic symmetry $\langle T_Z \rangle$ is negligible, but in a tetragonally distorted environment as well as at surfaces and interfaces $\langle T_Z \rangle$ becomes important. At the surface of Fe(001) and Ni(001) the value of

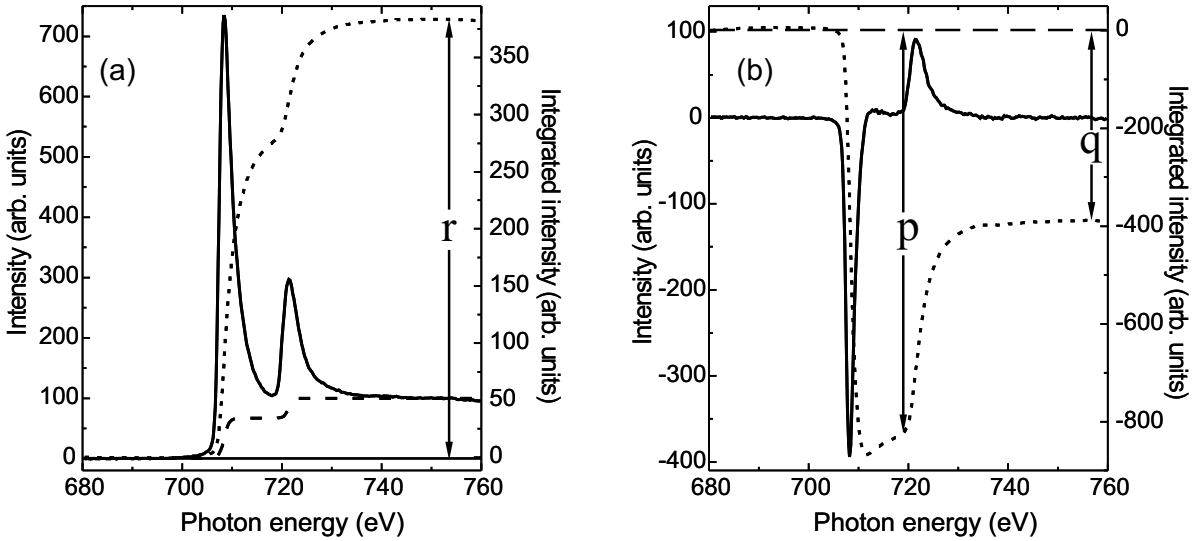

Figure 2.7: Isotropic absorption spectrum (a) and XMCD spectrum (b) (solid curves) and the corresponding integrals (dotted curves) of $Fe_4/Ni_{17}/Cu(100)$ at the Fe $L_{2,3}$ edges taken at 300 K. **r** equals the area between the isotropic spectrum and the step function (dashed curve) which simulates the contribution of photoelectrons being excited to continuum states.

$7\langle T_Z\rangle$ was calculated to equal $0.230\ \mu_{\mathrm{B}}$ and $-0.082\ \mu_{\mathrm{B}}$, respectively, compared to the values $0.028\ \mu_{\mathrm{B}}$ and $-0.027\ \mu_{\mathrm{B}}$ for Fe and Ni bulk-like layers [151].

The major source of errors on deriving the magnetic moments arises from the denominators of the sum rules, which correspond to the isotropic absorption cross section which is proportional to the number of holes n_h in the $3d$-shell. To eliminate the contribution from the s- and p-continuum states a double step function is subtracted from the isotropic absorption spectrum. This procedure ensures the validity of the sum rules, but it adds some arbitrariness to the determination of n_h in the final state. Calculations based on a high precision local density approach reveal that the orbital sum rule is valid within $5-10\%$, the error being due to sd-hybridization. For the spin sum rule the error due to hybridization is 15% for Fe and $40-50\%$ for Ni [151,152]. The ratio μ_L/μ_S is not affected by the error due to the uncertainty of n_h since both n_h and the isotropic absorption cross section are cancelled out. The determination of the single magnetic moments μ_L and μ_S requires a proper normalization of the absorption spectra as well as a correction of saturation effects, which occur if sampling of the electron yield is larger or comparable to the absorption depth of the incident x-rays [153]. Following the approach of [154] the magnetic moments μ_L and μ_S and their ratio are derived from experimental data by:

$$\mu_L = -\frac{2q}{3r}\,(10-n_{3d})\,\frac{1}{P_c\,\cos(\theta)} \tag{2.4}$$

$$\mu_S = -\frac{3p-2q}{r}\,(10-n_{3d})\,\frac{1}{P_c\,\cos(\theta)} + 7\langle T_Z\rangle \tag{2.5}$$

$$\frac{\mu_L}{\mu_S} = \frac{2}{9\left(\frac{p}{q}\right) - 6} \tag{2.6}$$

where p, q and r are the integrals denoting the area below the XMCD and the isotropic absorption spectra, respectively, as demonstrated in Fig. 2.7. P_c is the degree of circular polarization and θ indicates the polar angle measured between the wave vector $\mathbf{k}$ and the sample's normal $\mathbf{n}$. The number of electrons in the $3d$-band is given by n_{3d}, i. e. $(10 - n_{3d})$ is the number of unoccupied states in the $3d$-band.

2.2.2 Element-specific determination of the magnetization direction in bilayers

The orientation of the magnetization of a bilayer system like Fe/Ni/Cu(100) can be determined by polar-angular dependent XMCD measurements performed at the element-specific $L_{2,3}$ edges of Fe and Ni, respectively. A ferromagnetic coupling, and thus a common alignment of the magnetizations of Fe and Ni, results in an equal algebraic sign of the corresponding L_2 and L_3 edges of the XMCD spectra. In contrast, an antiferromagnetic coupling gives rise to an opposite sign of the corresponding edges reflecting the anti-aligned orientation of the individual magnetizations. Analogously, the shape of element-selective hysteresis loops of Fe and Ni will show the same magnetization reversal in the case of a ferromagnetic coupling and an opposite magnetization reversal of both elements if the coupling is antiferromagnetic.

The identification of the easy axis of the magnetization $\mathbf{M}$ requires sequent measurements at different polar angles θ. For an in-plane magnetized film there will be no dichroism at normal incidence of the x-rays ($\mathbf{k}\|\mathbf{n}$). The polar-angular dependent XMCD intensities of a perpendicularly magnetized film follow the law:

$$I(\theta) = I_\perp \cos(\theta) \tag{2.7}$$

where $I_\perp$ denotes the XMCD intensity for $\mathbf{k}\|\mathbf{n}$. In the case of a canted magnetization the components $M_\perp$ and $M_\|$ have to be measured in order to determine the polar angle α of $\mathbf{M}$ from $\tan(\alpha) = \frac{M_\|}{M_\perp}$. However, a grazing angle $\theta = 90°$ is not possible but $\theta = 80°$ can be used. In this case the canting angle α is determined by[2]:

$$\alpha = \arctan\Big(\frac{I_{||} - I_\perp \cos(\alpha)}{I_\perp \sin(\alpha)}\Big) \tag{2.8}$$

where $I_{||}$ denotes the XMCD intensity measured at a grazing angle of $\theta = 80°$. It should be noted that the correction of saturation effects becomes all-important at large angles θ. Alternatively, the absorption spectra can be measured by successively increasing θ from 0° to 80° and thus determining the angle, for which the XMCD signal is largest, indicating the direction of the magnetization.

[2]The details are given in the appendix A.6.

2.3 SQUID magnetometry

This chapter is restricted to a short introduction to the principles of operation of a radio frequency (rf)-SQUID. A detailed description of the fundamental physics of SQUIDs is given e. g. in [155]. The determination of the magnetization from the detected magnetic stray field is elucidated in section 2.3.2.

An rf-SQUID consists of a superconducting loop containing one weak link, i. e. a Josephson junction [156]. dc-SQUIDS which operate at a constant bias current have two Josephson junctions as described for example in [155]. A SQUID yields an output voltage signal which is a periodic function of the flux Φ penetrating the superconducting loop. By means of the critical temperature T_c, below which the material becomes superconducting, SQUIDs are further divided into two types: conventional low-T_c ($T_c < 10$ K) and high-T_c ($T_c > 10$ K) SQUIDs. While Niobium ($T_c = 9.25$ K) is a common material for low-T_c-SQUIDs, which must be cooled with liquid helium (lHe), high-T_c-SQUIDs are nowadays fabricated from $YBa_2Cu_3O_{7-x}$ (YBCO, $T_c = 93$ K) where the use of liquid nitrogen (lN_2) is sufficient to maintain $T < T_c$ [39,157]. The main advantage of the use of lN_2 is the lower cost and the easier handling compared to lHe. Due to their high sensitivity SQUIDs have found various applications, e. g. in the fields of non-destructive testing [158], magnetic microscopy [159], geophysics [160] and magnetocardiology [161].

2.3.1 Operation of an rf-SQUID

The electrical properties of the Josephson junction which is a thin insulating layer are determined by the two Josephson equations. The tunnel current I through the ideal barrier is limited by the critical current I_c which is given by the dc-Josephson equation:

$$I = I_c \sin\delta \tag{2.9}$$

where the relative phase $\delta = \Phi_1 - \Phi_2$ is determined by the phases Φ_i on the two sides of the junction. The associated superconducting order parameter is $\Psi = \Psi_0\, e^{i\Phi_i}$, and $|\Psi|^2$ equals the density of the Cooper-pairs. The ac-Josephson equation yields the voltage V across the ideal junction:

$$V = \frac{\hbar}{2e}\left(\frac{d\delta}{dt}\right) \tag{2.10}$$

In Fig. 2.8 (a) the inductive coupling of an rf-SQUID to the electronics is sketched. The real junction is illustrated by the equivalent circuit of the ideal, noise free junction, its physical capacitance and a resistor in a parallel connection, which accurately models the electrical properties of the SQUID [158].

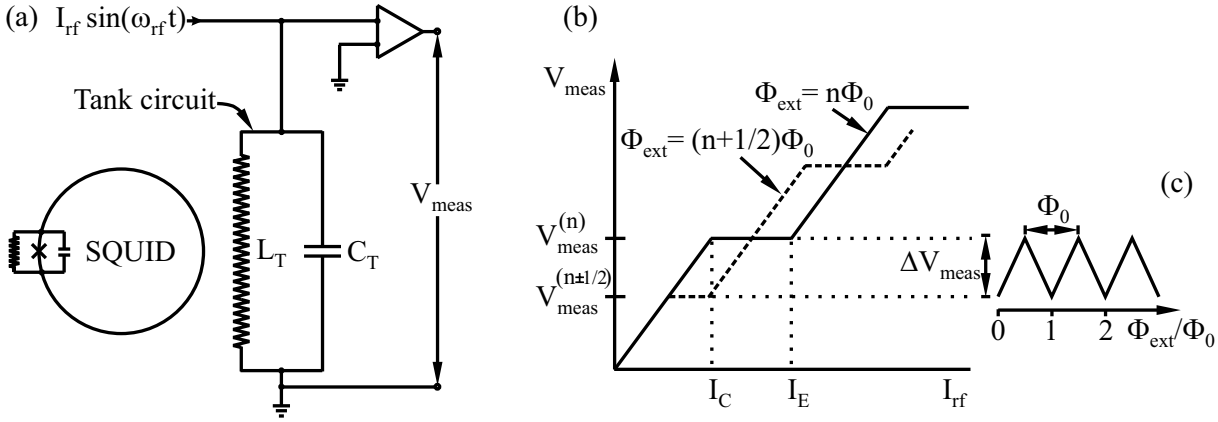

Figure 2.8: (a) Schematic of an rf-SQUID loop. The Josephson junction is marked by "×", and the loop is inductively coupled to an rf-tank circuit. The junction is shunted by a resistor, and its physical capacitance is shown as well. (b) Voltage V_{meas} drop at the tank circuit versus the bias current I_{rf} for the quantum states $\Phi_{\text{ext}} = n\Phi_0$ and $\Phi_{\text{ext}} = (n+\frac{1}{2})\Phi_0$. (c) Voltage-to-flux transfer function of the rf-SQUID. (After [163]).

According to the Bohr-Sommerfeld quantization constraint [162] a superconducting loop will contain flux only in multiples of the flux quantum, i. e. $n\Phi_0$, where n is any integer. A change in the flux Φ_{ext} applied to the SQUID will cause currents to oppose that change, resulting in a phase shift across the junction, which according to Eq. (2.10) gives rise to a voltage. The typical step function of the measured voltage V_{meas} versus the rf-current I_{rf} is depicted in Fig. 2.8 (b). V_{meas} increases linearly with I_{rf} until the current I_s, which is induced by the tank circuit reaches the critical current I_c. At this point a flux quantum jump occurs in the SQUID, and V_{meas} stays constant until the dissipation caused by the normal-conducting junction is compensated by $I_{\text{rf}} = I_E$ again [163]. The voltage-to-flux transfer function reveals a typical triangular shape as demonstrated in Fig. 2.8 (c).

2.3.2 Determination of magnetic moments from the stray field

The magnetic stray field of a thin film can be calculated by integrating elementary magnetic dipoles over the film area. A magnetic dipole $d\mathbf{m}$ in a distance $\mathbf{R}$ causes a field $d\mathbf{B}$, which is given by [2]:

$$d\mathbf{B} \;=\; \frac{\mu_0}{4\pi}\,\frac{(3\,\mathbf{n}\cdot d\mathbf{m})\,\mathbf{n} - d\mathbf{m}}{R^3} \tag{2.11}$$

where $\mathbf{n} = \mathbf{R}/R$ is a unit vector. Eq. (2.11) is based on the assumption that only magnetic dipoles contribute to the stray field, which is justified since the stray field is detected in a distance of approximately 5 mm. In this distance quadrupole- and higher order contributions are negligible since they vanish with higher powers of R^{-n} ($n = 5, 7, ...$).

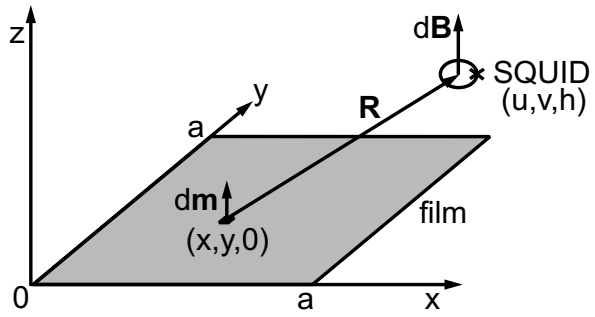

Figure 2.9: Coordinates and vectors used to calculate the stray field integrals.

For an in-plane magnetized square-shaped ultrathin film in the single domain state the z-component of the stray field after integration of Eq. (2.11) reads [164]:

$$B_z^{tot}(u,v,h) \;=\; \frac{3\mu_0}{4\pi}\, M\, d\, h \int\limits_{-a/2}^{a/2}\int\limits_{-a/2}^{a/2} \frac{u-x}{R^5}\; dx\, dy \tag{2.12}$$

where a is the width of the film, M the magnetization, d the film thickness, h the distance in which the stray field is detected and $\mathbf{R} = (u-x, v-y, h)$. The coordinates and vectors used to calculate the stray field integrals are given in Fig. 2.9.

The magnetic dipoles are assumed to have only an x-component m, i. e. $d\mathbf{m} = (m, 0, 0)$, and they are located at the position $(x, y, 0)$ in the film plane. All contributions to the magnetization are projected onto the x-axis which is the easy axis of the film. The detection of the stray field along the x-direction in a constant distance h and in a centered position ($v = 0$) yields the field distribution of $B_z(u, v, h)$ shown in Fig. 2.10 (a). The position and the shape of the two peaks are affected by h and a as discussed elsewhere [39,165], whereas their peak-to-peak value is determined by h, d and M. Since the magnetization is the only unknown parameter, the value of M can be derived from applying Eq. (2.12) with M as a fit parameter to a SQUID measurement. Knowing the crystal structure of the film and the inter- and intralayer spacing of the atoms, the total magnetic moment per atom can be obtained.

For a perpendicularly magnetized ultrathin film where $d\mathbf{m} = (0, 0, m)$ Eq. (2.12) changes to:

$$B_z^{tot}(u,v,h) \;=\; \frac{\mu_0}{4\pi}\, M\, d \int\limits_{-a/2}^{a/2}\int\limits_{-a/2}^{a/2} \frac{3h^2}{R^5} - \frac{1}{R^3}\; dx\, dy \tag{2.13}$$

An exemplary calculation of the stray field distribution according to Eq. (2.13) for an out-of-plane magnetized 3 ML Fe film is demonstrated in Fig. 2.10 (b). The numerical solutions for Eq. (2.12) and Eq. (2.13) can be found in [39]. In conclusion, the decrease of the distance h from 6 mm to 4 mm enhances the signal by a factor of ≈3. This indicates that the smallest possible distance is required in order to achieve the maximum signal-to-noise ratio of a ferromagnetic monolayer. Since the equations 2.12 and 2.13 are based on a homogeneously

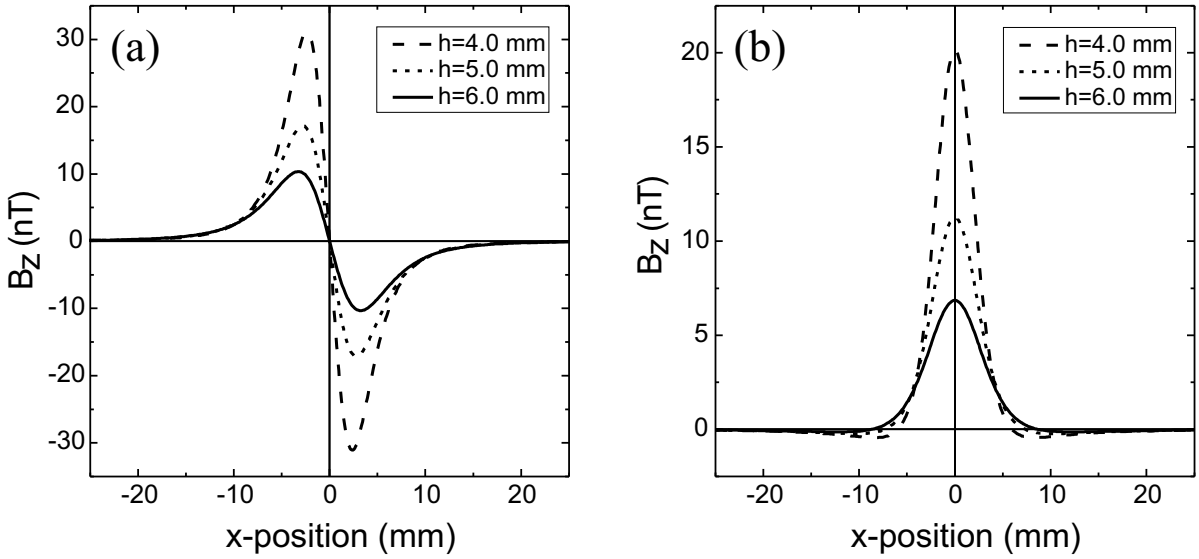

Figure 2.10: Calculated stray field distribution of a homogeneously magnetized rectangular-shaped ultrathin Fe film of 3 mm width and a magnetization of 1740 kA/m for different distances h. The calculation (a) according to Eq. (2.12) corresponds to an 11 ML in-plane magnetized Fe film, and (b) shows the calculation according to Eq. (2.13) for a 3 ML perpendicularly magnetized Fe film.

magnetized perfectly rectangular sample, only the stray field component B_z of *in situ* grown rectangular-shaped films can be simulated. Possible deviations of the measured stray field distribution from the calculation may arise from closure domains at the edges of the film, which are not considered in the above theory.